Strain-rate and off-axis loading effects on the fibre compression strength of CFRP laminates: Experiments and constitutive modelling

Daniel Thomson [a,*], Gustavo Quino [a], Hao Cui [b], Antonio Pellegrino [a], Borja Erice [a,c,d], Nik Petrinic [a]

[a] Department of Engineering Science, University of Oxford, Oxford, United Kingdom
[b] School of Aerospace, Transport and Manufacturing, Cranfield, United Kingdom
[c] Structural Impact Laboratory (SIMLab), Department of Structural Engineering, Norwegian University of Science and Technology (NTNU), NO-7491, Trondheim, Norway
[d] Centre for Advanced Structural Analysis (CASA), Department of Structural Engineering, NTNU, NO-7491, Trondheim, Norway

A B S T R A C T

A series of dynamic longitudinal compression tests have been performed on cross-ply IM7/8552 specimens cut at different off-axis angles to produce different combinations of compression and shear stresses. Together with results from previous quasi-static tests of the same kind, quasi-static and dynamic fibre kinking failure envelopes have been obtained using classical laminate theory. This new experimental data has been compared against predictions from the leading fibre kinking theories, made rate-dependent by using rate-dependent in-plane shear properties, and show that, while they can accurately predict the effects of strain rate on the uniaxial compression strength, they are unable to capture the effects of shear, neither at quasi-static nor dynamic rates. Instead, a simpler more phenomenological approach is proposed to predict the rate-dependent fibre kinking strength of FRP laminates under multi-axial loads until the micromechanics can be more accurately described.

1. Introduction

Longitudinal compressive failure in carbon fibre-reinforced polymer (CFRP) laminates, or fibre kinking, is arguably the most complex failure mechanism observed in these materials. There has been much work done over the years to understand the micro-scale mechanisms behind this type of failure and, while it is now widely recognised as a form of buckling instability in the fibres driven by the response of the supporting matrix, there are still specific aspects of the micromechanics that remain to be explained. Leading fibre kinking theories, such as those by Budiansky and Fleck [1,2] and Pinho [3,4], can accurately predict failure under uniaxial compression given the initial misalignment or waviness of the fibres and the nonlinear shear response of the laminate. However, under multi-axial loading, different models start to give diverging predictions based on how they address the evolution of fibre misalignment under transverse stresses [5]. In addition, even some of the aspects where all models agree have yet to be fully verified experimentally, such as the effects of strain-rate or temperature.

Matsuo and Kageyama [6] recently showed that the effects of temperature on the uniaxial compression strength of a thermoplastic CFRP composite were in good agreement with the predictions from Fleck's fibre kinking theory, where the change in strength was directly related to the change in the nonlinear shear response of the laminate. However, due to the complexity of the experimental procedures, very little work has been done to characterise the longitudinal compression behaviour of CFRPs under off-axis and dynamic loads, which is crucial for a more extensive validation of these fibre kinking models, especially for impact loading applications where the material is subjected to multi-axial stresses and high strain-rates.

Based on recent work by the authors [5], who proposed an improved testing methodology to measure the uniaxial and off-axis compressive strength of CFRP laminates using cross-ply (CP) specimens, and previous work by Ploeckl et al. [7], who showed a roughly 40% increase in the uniaxial compression strength of a quasi-isotropic (QI) laminate from quasi-static to high strain-rate testing, the work presented here aims to investigate the effects of strain-rate on the fibre kinking failure envelope by testing the same IM7/8552 CFRP from Refs. [5] under high-rate off-axis compression.

Finally, the obtained experimental data was used to evaluate the accuracy of different fibre kinking theories under quasi-static and

dynamic multi-axial loading.

2. Methodology and experimental set-up

Following the quasi-static study in Refs. [5], a series of dynamic off-axis compression tests have been performed using a similar cross-ply specimen configuration and data reduction methods to extract the longitudinal compression strength from the axial measurements.

The specimens were tested at high strain-rates using a Split-Hopkinson Pressure Bar (SHPB) system, described in section 2.2, and longitudinal ply failure data was extracted from the specimen strengths using Classical Lamination Theory (CLT), following the methodology described in Ref. [5,8].

2.1. Specimen configuration

Based on the previous work in Ref. [5], cross-ply material was selected over thick unidirectional (UD) material, however, some minor modifications to the quasi-static specimen design were necessary. The rectangular specimen design used for quasi-static testing in Ref. [5] was found not to be suitable for dynamic testing, exhibiting premature cracking and specimens rotating out of place during loading. Instead a tabbed dog-bone design was used as shown in Fig. 1. The screwed end caps fitted into the SHPB input and output bars ensured specimen alignment throughout the test, while the dog-bone design mitigated the effects of noise and stress concentrations at the specimen-bar interfaces.

All specimens were cut from a 10 mm $[0/90]_{20S}$ IM7/8552 [9] plate using a water jet cutter and were ground down to the final specifications, detailed in Fig. 1. For the uniaxial compression tests, specimens were cut parallel to the fibre direction of the external plies and additional specimens were prepared at 3°, 6°, and 10° to the surface fibre direction in order to produce different combinations of longitudinal compression and shear stresses.

Due to the excessive thickness of the cross-ply laminates, a dog-bone shape was also ground in the out-of-plane direction, Fig. 1 a), to achieve the desired cross-section of 16 mm^2. It should be noted that a simpler dog-bone specimen design, Fig. 1 b), without the out-of-plane grinding was also tested using a different material and produced equally reliable results. The more complex design used for the IM7/8552 composite was only necessary to reduce the thickness of the source material in order to facilitate the achievement of dynamic loading rates and material failure during SHPB experiments.

In order to ensure alignment throughout the test and avoid the introduction of spurious loading pulses, the specimens were bonded to M12 threaded end caps using a 3M DP490 adhesive, allowing them to be fitted into the M12 threaded holes in the input and output bars of the SHPB, which were supported by low friction PTFE bushings at a pitch of 300 mm.

Finally, since the fibre kinking strength is known to be strongly dependent on the fibre misalignment, one of the 6° specimens was used to characterise the microstructure of the laminate following the procedure from Ref. [10]. By this approach, a fibre's orientation, α, with respect to a cutting plane can be obtained from the length of the fibre's elliptical cross-section, l_e, and the fibre diameter, d_f, as illustrated in Fig. 2 a):

$$\sin(\alpha) = \frac{d_f}{l_e} \tag{1}$$

The 6° cross-ply specimen was polished using 1 μm water-based polycrystalline diamond suspension and analysed under an optical

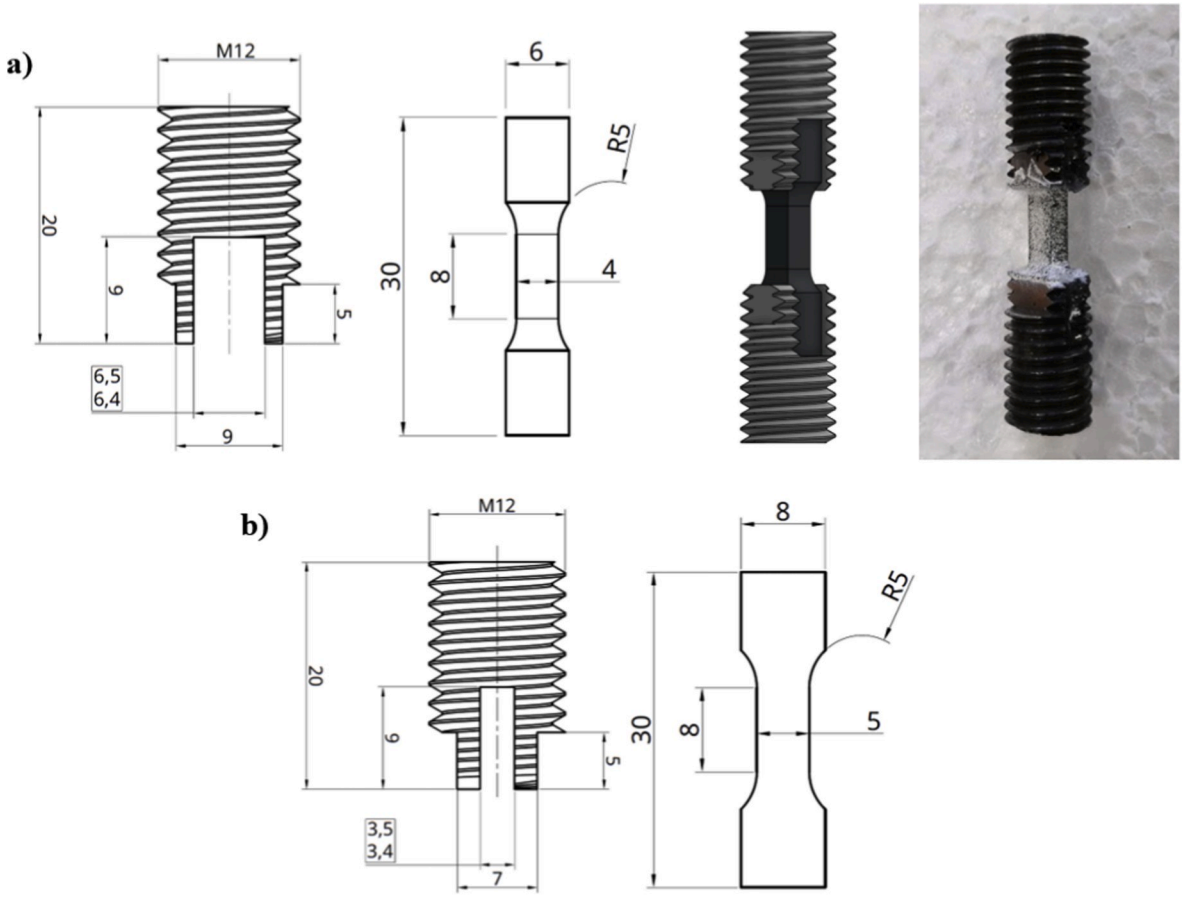

Fig. 1. *Cross-ply specimen and end cap design for dynamic loading. a) IM7/8552 specimens from* 10 mm *initial plate thickness used in this study, b) simpler specimen successfully tested for a* 3 mm *thick plate with only in-plane dog-bone. Dimensions in mm.*

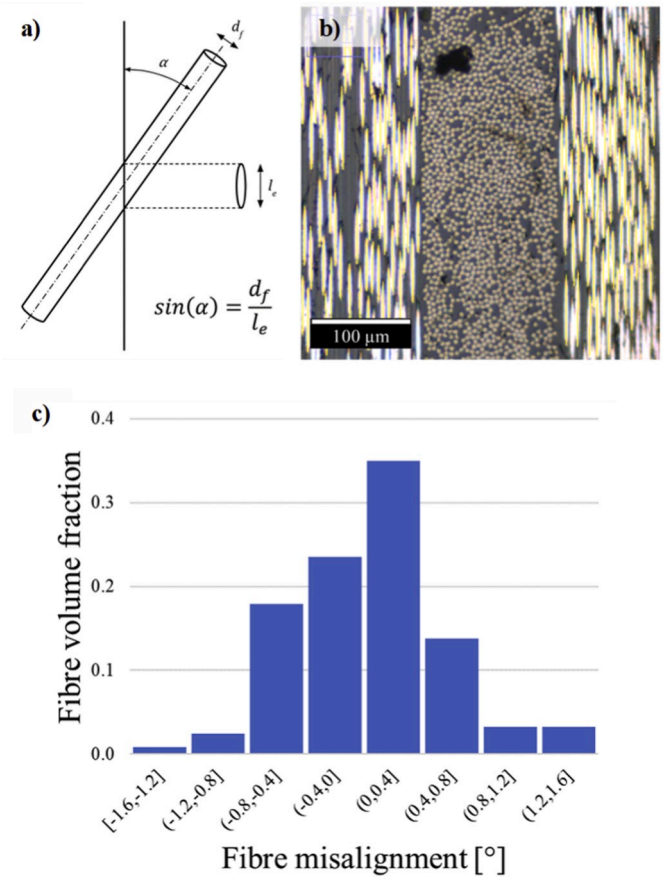

Fig. 2. *a) Illustration of the relation between the length elliptical fibre cross-section, l_e, and the angle of the cutting plane, α. b) Optical microscopy of a cross-ply specimen with a 6° cutting plane. c) Histogram of the measured fibre misalignment distribution.*

microscope, Fig. 2 b), in order to measure the distribution of fibre orientations in the material. A representative area of the 6° cutting plane was selected and the length of the elliptical cross-section of 123 individual fibres was measured using the image processing software imageJ [11]. The fibre diameter, 5.2 µm, is given by the supplier [12] and was verified in the same way through optical microscopy. With this, the orientation of the measured fibres was determined using eq. (1) in order to obtain the distribution of fibre misalignment with respect to the mean. The results showed the fibre misalignment was within ±1.6°, with a standard deviation of 0.52°, which is in is in line with typical values for modern CFRPs [13,14]. A histogram of the fibre misalignment is shown in Fig. 2 c).

2.2. *Experimental set-up and data reduction*

With the specimens fully prepared and mounted, an SHPB system like the one described in Ref. [15] was used to apply a high strain-rate compressive pulse through the material. The system consists of the 16 mm titanium striker, input and output bars detailed in Fig. 3 a) and the alignment and containment chamber shown in Fig. 3 b). The striker is fired from a compressed air chamber at the input bar creating the compressive pulse. A 1 mm rubber pulse shaper was used between the striker and input bar to produce a gentle rising edge in the compressive wave and facilitate the achievement of dynamic equilibrium conditions. The specimens were screwed into both the input and output bars, as described in section 2.1 above, and strain gauges mounted along the bars, indicated by the 'SG' symbols in Fig. 3 a), measured the stress waves travelling into and out of the specimen. This allowed for forces at the input and output interfaces of the specimen to be computed using one-dimensional wave propagation theory. Once dynamic equilibrium was established for each test, the axial strains and stresses were computed using the specimen dimensions measured before the experiment.

The tests were recorded using a Kirana high-speed camera by Specialised Imaging at 500.000 fps and a resolution of 924 × 768 pixels

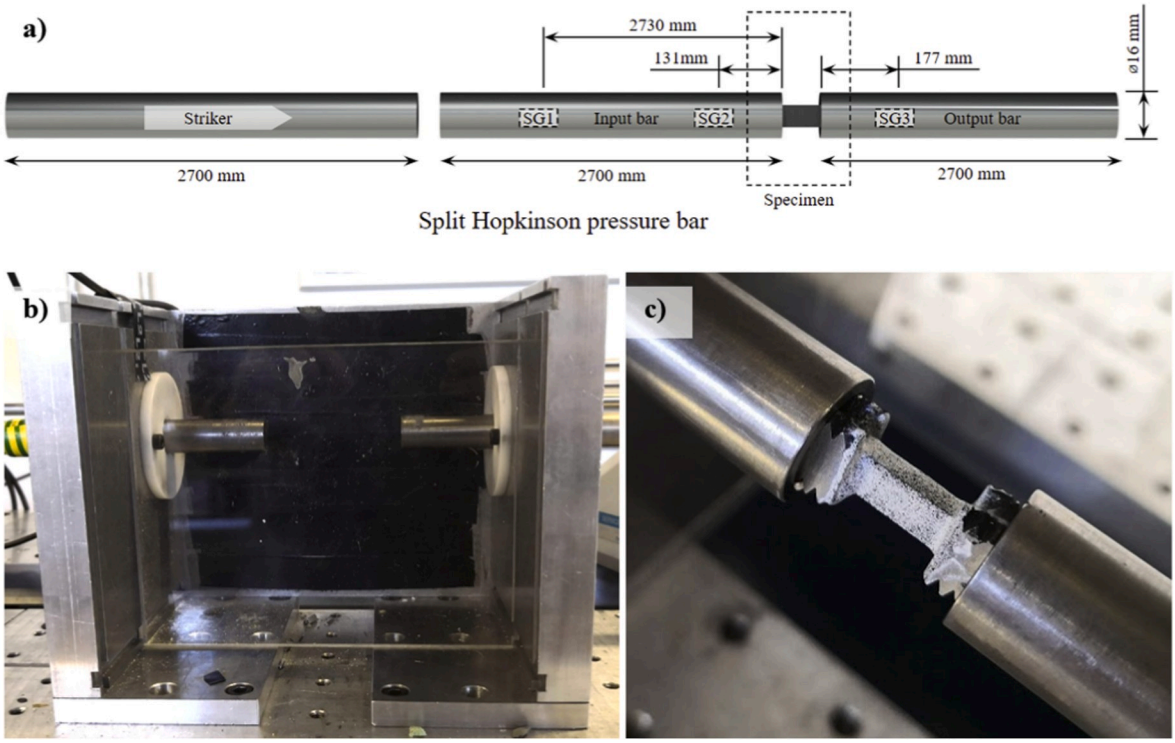

Fig. 3. SHPB test set-up used for the dynamic compression tests. a) schematic of the SHPB system, b) alignment and containment fixtures, and c) inserted specimen with speckle pattern for DIC.

covering an area of approximately 30 mm × 25 mm. This allowed for the full strain field data to be obtained through digital image correlation (DIC), which was used to validate the strain gauge measurements and verify that adequate testing conditions were met. For this purpose, a fine speckle pattern was applied to all specimens, as shown in Fig. 3 c). Finally, the camera was also connected to the oscilloscope used to record the signal from the strain gauges in order to synchronise the strain and force histories.

With the above in place for all specimens, the tests were fired with a pressure of approximately 1 bar for a striker velocity of around 6 m/s, producing strain-rates in the order of 100 s^{-1}. In these conditions, the tests lasted between 0.2 and 0.3 ms before specimen failure, which was well before any stress wave reflections could reach the strain gauges and allowed for 100 to 150 images to be captured for the DIC analysis.

3. Results

With the updated dynamic specimen design, the stress concentration and boundary effect issues observed in previous iterations were successfully avoided. The results, summarized in Fig. 4 and Table 1 below, showed good repeatability and the stiffnesses were in good agreement with the quasi-static results from Ref. [5], giving confidence in the data acquisition and processing methods. Fig. 4 shows the obtained axial stress-strain curves for each of the four specimen orientations compared to the quasi-static data. A summary of the strength data for all quasi-static and dynamic tests is given in Table 1. On average, a strain-rate of 75 s^{-1} was achieved for the 0° uniaxial compression tests with this number increasing slightly in the off-axis tests as the axial stiffness decreased. The initial noise observed in some of the dynamic curves in Fig. 4 is attributed to the error in the stress calculations before dynamic equilibrium was reached and does not affect the rest of results.

While these results will be analysed in more depth in the following sections, an increase in strength with regard to the quasi-static data is immediately visible across all specimens. In addition, the 10° specimens are noticeably lacking any significant nonlinear behaviour in the dynamic tests, Fig. 4 d). Both of these differences can be attributed to the viscous stiffening and hardening of the matrix at higher strain-rates, which has been observed in Ref. [16].

Furthermore, as all tests showed linear stress-strain behaviour up to the point of failure, linear CLT could be used to extract longitudinal ply stresses from the axial data, following the procedure described in Refs. [5,8]. This allowed for the longitudinal compression stress, σ_{11}, and in-plane shear stress, τ_{12}, in the longitudinal plies to be determined from the axial strength for each type of specimen, producing the failure envelopes shown in Fig. 5. Because the quasi-static 10° tests showed significant nonlinear behaviour, the data obtained using linear CLT is less reliable and is shown in light grey in the plot.

The new high strain-rate results in Fig. 5 follow a similar trend to the previous quasi-static data as well as some of the biaxial loading data found in the literature [17,18]. The longitudinal compression strength can be seen to decrease in an apparent linear trend as the shear stress increases but, as will be discussed in the following sections, the off-axis specimens still maintained significant strength in the 11 direction even at high amounts of shear, contradicting some of the leading fibre kinking theories. In addition, as mentioned above, a significant increase in strength with respect to the quasi-static data can be observed across all specimen orientations. This increase was around 20–35% for strain-rates of 75–85 s^{-1}, matching what was reported by Ploeckl et al. [7] for the uniaxial compression strength of a quasi-isotropic laminate.

Although, due to severe fragmentation, none of the specimens were in suitable conditions for post-mortem imaging to verify that they did indeed fail due to fibre kinking, the results from the quasi-static campaign and the repeatability of the new dynamic results should give enough confidence that the test results are valid. For reference, scanning electron microscope (SEM) images of fibre buckling in three of the QS specimens from Refs. [5] are shown in Fig. 6. It is interesting to

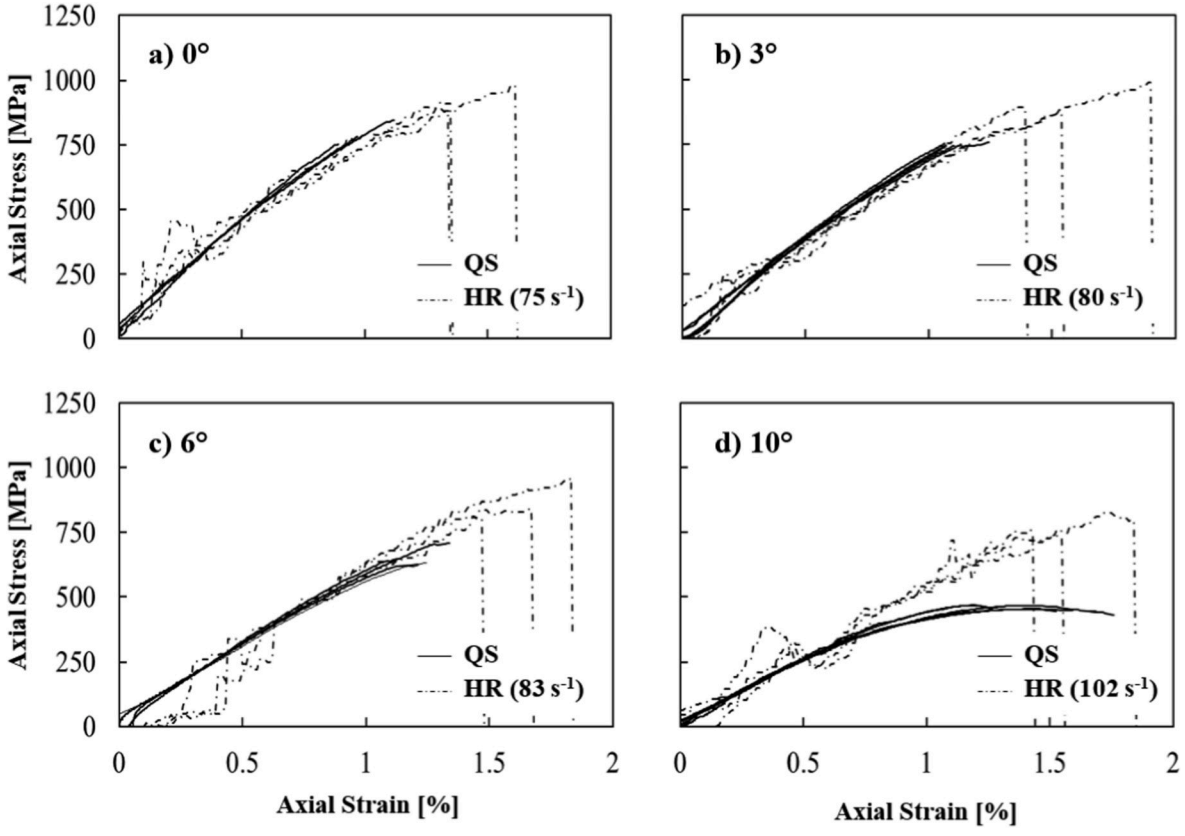

Fig. 4. Axial stress-strain curves obtained for each of the CP specimen orientations at quasi-static (QS) and dynamic (HR) loading rates.

Table 1
Summary of off-axis (0, 3, 6, and 10°) axial strength results at quasi-static (QS) and dynamic (HR) strain-rates. Average strain-rates (SR) are given in legend in s^{-1}.

Axial Strength	0° QS [MPa]	0° HR [MPa]	3° QS [MPa]	3° HR [MPa]	6° QS [MPa]	6° HR [MPa]	10° QS [MPa]	10° HR [MPa]
1	747	925	744	911	623	959	467	828
2	783	903	746	1001	643	814	468	823
3	847	986	741	900	706	873	452	798
4					630		451	
5							466	
AVG	792	938	744	937	651	882	461	816
STDV	50.6	43.1	2.1	55.3	37.9	73.4	8.5	15.9
CV (%)	6.4	4.6	0.3	5.9	5.8	8.3	1.9	1.9
SR [s^{-1}]	1E-3	75	1E-3	80	1E-3	83	1E-3	102

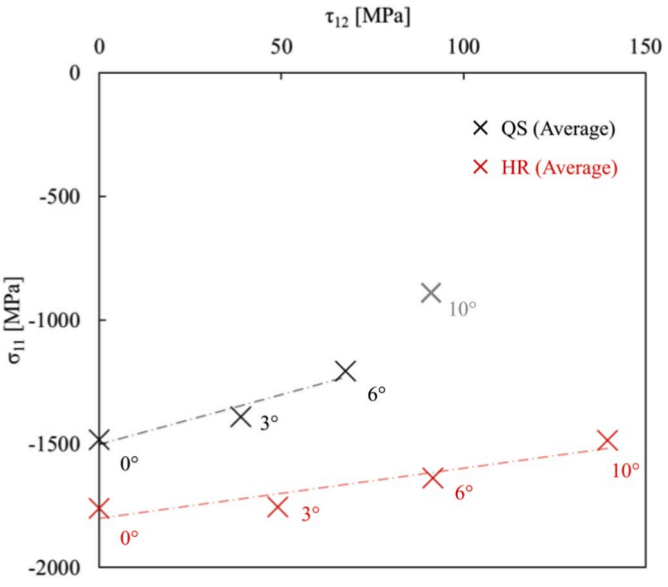

Fig. 5. Quasi-static (QS) and dynamic (HR) failure envelopes extracted from axial strength data using linear CLT. X marks indicate the average strength for each specimen type and the dotted lines show the linear trend for each data set.

note that there appears to be a change from out of plane buckling in the 3° and 6° specimens to in-plane buckling in the 10° specimen, likely caused by the increasing in-plane shear stresses.

In addition, images from the high-speed camera, as shown for one of the tests in Fig. 7, indicate that specimen failure was caused by the initial collapse of the external longitudinal plies, which are presumed to have buckled due to fibre kinking.

4. Analysis and discussion

With these new experimental results, a comprehensive set of fibre kinking failure data for one same material system at different loading rates and biaxial stress states was compiled, which has been used to evaluate some of the leading failure theories and criteria. In particular the analytical model by Budiansky and Fleck [1,2] and the numerical 3-dimensional implementation by Pinho for the NASA LaRC criteria [3, 4,19] have been compared.

4.1. Strain-rate effects

While none of the following models were explicitly developed with rate-dependency in mind, they can be adapted for dynamic loading relatively easily. These models all have in common that they predict fibre kinking failure based the nonlinear shear stress-strain response of the composite. If the nonlinear shear properties are made rate-dependent, the same criteria will be able to give predictions for different dynamic strain-rates. Following the approach used in Ref. [20–22], the in-plane shear properties of the composite can be scaled by a function $r(\dot{\varepsilon})$ to obtain different dynamic values for each strain-rate, $\dot{\varepsilon}$:

$$r(\dot{\varepsilon}) = 1 + \sqrt{K\dot{\varepsilon}} \tag{2}$$

Using the quasi-static and dynamic data from Ref. [23], a Ramberg-Osgood nonlinear shear relation [24], eq. (3), and two rate-dependent parameters for the shear modulus and yield stress, K_G and K_y, were calibrated for the IM7/8552 material so that the different curves for rates between 75 and 100 s^{-1} could be obtained and used with the models described in the following sections. While only strain rates in the order of 100 s^{-1} have been investigated here, the validity of the above approach is tied to the validity of the nonlinear shear curves so the following criteria could potentially be used up to rates around 300 s^{-1} with the given material properties. The used material parameters are given in Table 2 and the resulting stress-strain curves are illustrated in Fig. 8.

$$\gamma = \frac{\tau}{G}\left[1 + k\left(\frac{\tau}{\tau_Y}\right)^{n-1}\right] \tag{3}$$

4.2. Analytical fibre kinking theory

Currently, the most advanced fibre kinking theories are based on the original work by Rosen [25], where failure was predicted as elastic micro-buckling using a beam buckling model for parallel, perfectly aligned columns in an elastic medium. This gave a compressive strength of the form:

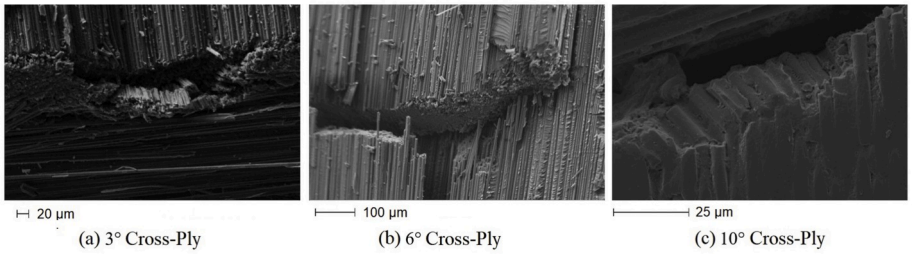

Fig. 6. *SEM images of fibre buckling from different QS cross-ply specimens* [5].

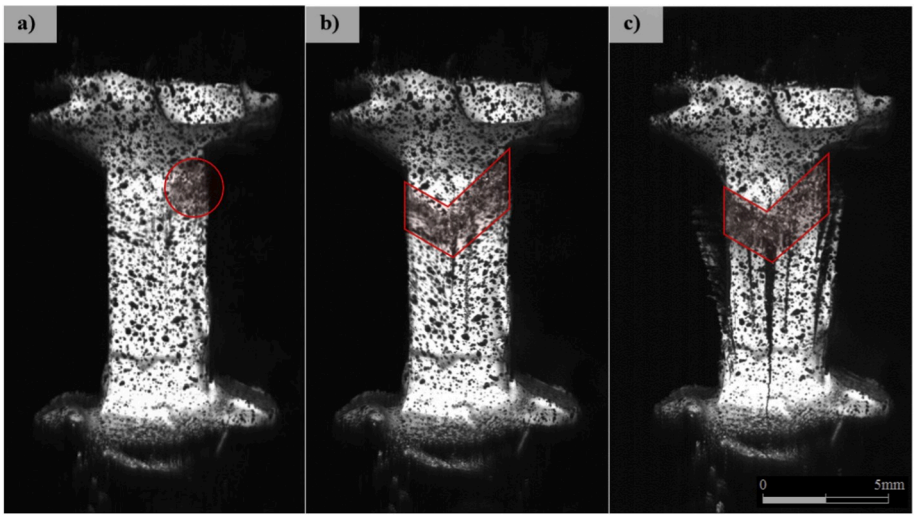

Fig. 7. *High-speed camera images of a 6° specimen at the point of failure with a* 5 mm *scale bar. Failure can be seen to initiate in the highlighted outer longitudinal plies in a) and propagate through the rest of the specimen in b) and c).*

Table 2
Ramberg-Osgood nonlinear shear properties and rate-dependent scaling parameters calibrated for IM7/8552 from the data given in Ref. [23].

G [MPa]	K_G	τ_y [MPa]	K_y	k	n
5000	3E-4	85	1.5E-3	0.43	5.8

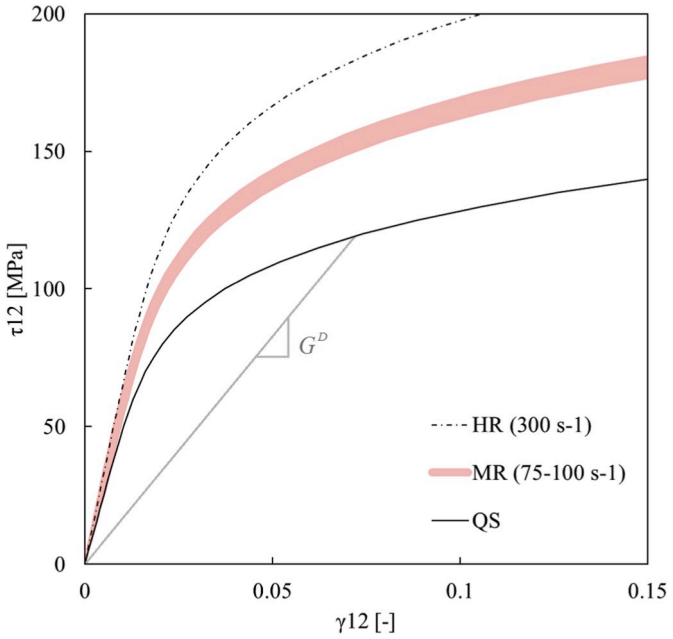

Fig. 8. *Shear stress-strain curves for IM7/8552 composite at quasi-static (QS) and dynamic (HR) strain-rates reproduced from* Ref. [23]. *The intermediate rate curve (MR) is extrapolated from the other two using eq. (2) from* Ref. [20–22].

$$\sigma_C = \frac{G_b}{(1-v_f)} = G \tag{4}$$

where G_b is the shear modulus of the matrix and v_f the fibre volume fraction, resulting in a compressive strength equivalent to the shear modulus of the composite G, which severely over-predicted the strength of the material.

In 1972, Argon [26] argued that composites undergo plastic rather than elastic micro-buckling, with kinking occurring due to misaligned fibres, so that the compressive strength was obtained as a function of the yield stress in shear and the initial misalignment of the fibres. This gave improved but not quite accurate predictions and paved the way for the work by Budiansky and Fleck [1,2], who built on these previous theories to include the effects of fibre rotation and nonlinear shear behaviour in the matrix by solving the equilibrium of the assumed kink-band geometry, shown in Fig. 9.

For the case of combined longitudinal compression, σ^∞, and in-plane shear, τ^∞, the following equilibrium relation can be obtained:

$$\sigma_C - 2\tau^\infty \tan\beta = \max\left(\frac{\tau - \tau^\infty + \sigma_T \tan\beta}{\varphi + \bar{\varphi}}\right) \tag{5}$$

which, for the specific case of uniaxial loading ($\tau^\infty = 0$), results in a direct analytical expression for the critical compressive stress, σ_{C0}, at which the fibres will buckle:

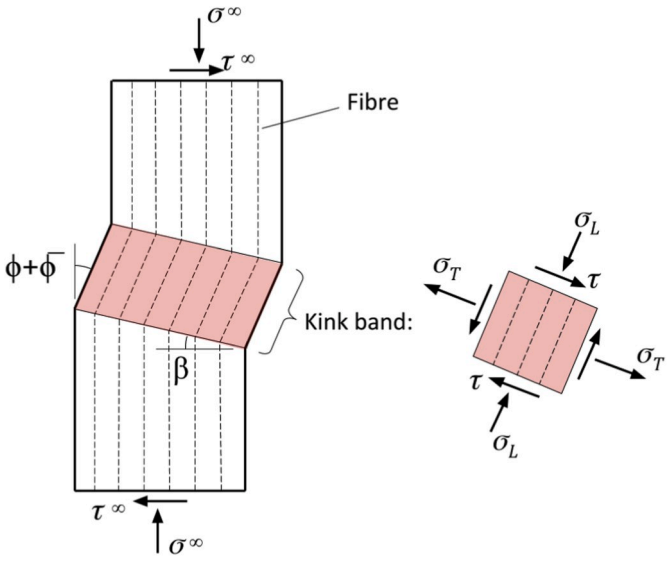

Fig. 9. *Typical kink band geometry and notation assumed by Budiansky and Fleck* [1,2].

$$\sigma_{C0} = \frac{G^*}{1 + nk^{1/n}\left(\frac{\overline{\varphi}/\gamma_Y^*}{n-1}\right)^{(n-1)/n}} \tag{6}$$

with $G^* = \alpha^2 G$, $\gamma_Y^* = \gamma_y/\alpha$, and $\alpha = \sqrt{1 + \left(\frac{\sigma_{TY}}{\tau_Y}\right)^2 \tan^2\beta}$. Where G is the shear modulus of the composite, $\overline{\varphi}$ is the initial fibre misalignment and β the kink band angle; σ_{TY} and τ_Y are yield stresses in transverse tension and shear; and n, k are Ramberg-Osgood [24] parameters for the nonlinear shear response of material, which is made rate-dependent by scaling the yield stress and shear modulus with eq. (2).

For off-axis compression, however, the solution becomes more complicated and cannot be found analytically. Instead, an iterative approach, described in detail in Ref. [1], must be used.

The iterative solution for combined compression and shear was implemented in MATLAB with a rate-dependent Ramberg-Osgood equation for the nonlinear shear response using eq. (2) as shown in Fig. 8 to obtain the analytical failure envelope for quasi static and dynamic loading at strain-rates of 75–100 s^{-1}. The initial fibre misalignment was calibrated from the quasi-static uniaxial compression test. For the given nonlinear shear properties, a misalignment angle of approximately 1.6° was obtained, in line with the previous microstructural characterisation results, and was then used to predict the off-axis quasi-static and all dynamic strengths. The predicted envelopes are plotted against the experimental results from section 3 in Fig. 10 below. As can be observed, the uniaxial compression prediction using Budiansky and Fleck's solution scales very well with the strain-rate, similar to Matsuo and Kageyama's observations on its ability to predict the effects of temperature [6]. Interestingly, however, the effects of shear in the off-axis compression cases are over predicted, excessively lowering the longitudinal strength in both the quasi-static and dynamic envelopes. Even using the extended analytical solution from Ref. [1,27], which also accounts for the effects of transverse compression, σ_{22}, the off-axis predictions were not significantly improved.

4.3. LaRC failure criteria

Building on the above, Pinho [3,4,19] developed a numerical implementation of Fleck's kinking theory adapted for more general 3-dimensional loading, whereas Fleck's solutions in Ref. [1,2] were only derived for in-plane loading conditions. In Pinho's LaRC model, a three-dimensional stress state is rotated onto the fibre misalignment frame, where matrix failure and fibre stability criteria are evaluated through iteration. Shear stresses in the rotated frame contribute to additional fibre rotation, which, in turn, may increase the shear stress in the misalignment frame. If a stable solution can be found, potential failure of the matrix is then evaluated using Inter-Fibre Fracture (IFF) criteria of the form:

$$\begin{cases} f_{kink} = \left(\frac{\tau_T}{S_T - \mu_T\sigma_n}\right)^2 + \left(\frac{\tau_L}{S_L - \mu_L\sigma_n}\right)^2 = 1 & for \quad \sigma_b \le 0 \\ f_{kink} = \left(\frac{\sigma_n}{Y_T}\right)^2 + \left(\frac{\tau_T}{S_T}\right)^2 + \left(\frac{\tau_L}{S_L}\right)^2 = 1 & for \quad \sigma_b > 0 \end{cases} \tag{7}$$

where σ_b is the transverse stress on the misalignment frame; σ_n, τ_T and τ_L are normal and shear stresses on the IFF plane; and Y_T, S_T and S_L are the normal and shear strength properties of the composite, with frictional parameters μ_T and μ_L. An in-depth explanation of this implementation and the theory behind it is given in Refs. [3,4,19].

As with Fleck's analytical model in section 4.2, an implementation of the LaRC model was used to obtain quasi-static and dynamic failure envelopes using the uniaxial compression case for calibration along with the rate-dependent nonlinear shear properties and, in this case, rate-dependent IFF strength parameters taken from Ref. [23]. For the same initial misalignment of approximately 1.6° used with Fleck's criterion, the results are shown in Fig. 10 next to the experimental data and Fleck's analytical predictions.

As expected, the LaRC predictions for the uniaxial compression case are almost identical to the analytical ones. However, the two envelopes begin to diverge with off-axis loading due, primarily, to: a) different assumptions regarding the kink band angle, β, between the two; and b) the fact that the LaRC model not only considers stability of the rotating fibres in the kink band, but also considers potential inter-fibre fracture (IFF) failure in the matrix if a stable rotation is achieved. Furthermore, while these differences cause a more pronounced drop in the strength under off-axis loading compared to Fleck's solution, they are arguably more physically sound, at least with regards to the treatment of potential matrix failure.

In any case, regardless of the minor differences between them, the shortcomings in both the previous models highlight the need for a better description of the fibre kinking failure mechanisms under off-axis compression loads. However, without a deeper look into the micromechanics of the problem, any potential changes to the underlying assumptions of the fibre kinking theory under off-axis loading would lack the strong physical basis of the uniaxial compression theory. One way forward may be micromechanical modelling of the kind done by Naya et al. in Ref. [28] and a similar study including off-axis loads could shed some light on the effects of shear on fibre rotation within the misalignment frame.

Keeping in mind the above concerns, a potential improvement to the fibre kinking model for off-axis compression cases is investigated in the following section.

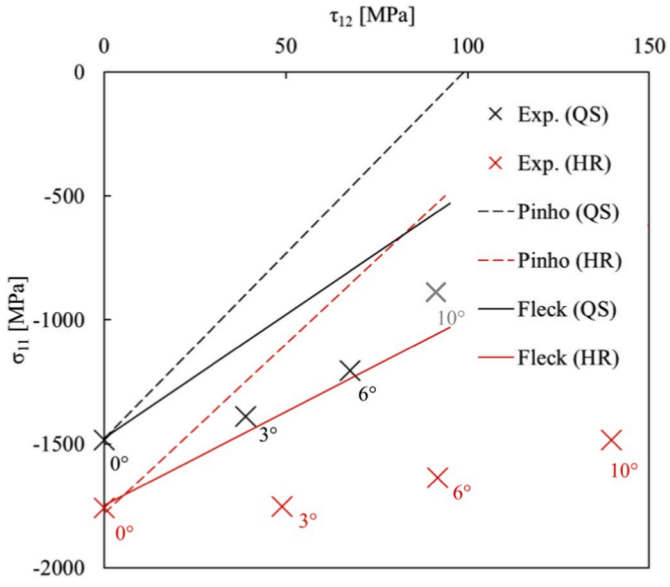

Fig. 10. *Experimental quasi-static (QS) and dynamic (HR) data compared against predictions from Pinho's LaRC criteria [3,4,19] and Budiansky and Fleck's analytical solution for longitudinal compression and shear [1,2].*

4.4. Shear damage model

Given that the 0° predictions in the previous sections are accurate and Budiansky and Fleck's fibre kinking theory [1,2] been extensively validated in the past for uniaxial compression cases, it seems that any inaccuracies in the off-axis predictions must come from the additional assumptions made for the effects of off-axis loads.

Under Budiansky and Fleck's assumed fibre kinking equilibrium and kinematics for the of off-axis loading case, any remote shear stress, τ^∞, would increase the waviness or additional rotation, φ, of the misaligned fibres. This additional rotation is what causes the reduction in the strength under increasing shear stress and in Ref. [1,2] was accounted

for by an additional shear knockdown factor that reduced the uniaxial compression strength from eq. (6).

Therefore, the most likely cause for the under prediction of the off-axis compression strength in the previous sections is an over-estimation of the additional rotation, φ, in the misaligned fibres caused by the remote shear, τ^{∞}.

While further research would be necessary in order to confidently establish the micromechanics for the off-axis loading case, as an initial approximation and as a way to test the above hypothesis, it has been assumed instead that the effects of off-axis loads on the fibre waviness are negligible.

By neglecting this effect on the critical misalignment angle, the off-axis compression case can be treated in a simplified manner as the superposition of: (a) a uniaxial compressive load with no change to the fibre misalignment or the kinematics of the misaligned fibres, which is predicted by Fleck's uniaxial compression strength criterion, σ_{C0}, in eq. (6); and (b) an of off-axis load that may introduce matrix damage in the material, affecting the nonlinear shear behaviour.

Therefore, under these assumptions, the off-axis compression case can be considered as a case of uniaxial compression where the shear properties of the material may have been degraded by the off-axis loads. In this way, the off-axis compression strength can then be approximated by using eq. (6) for the uniaxial compression strength with damaged shear properties corresponding to the applied off-axis loads. By replacing the shear modulus, G, in eq. (6) with the damaged modulus, G^D, the off-axis compression strength becomes:

$$\sigma_C = \frac{G^D}{1 + nk^{1/n}\left(\frac{\overline{\varphi}/\gamma_Y^*}{n-1}\right)^{(n-1)/n}} = \frac{G(1-D)}{1 + nk^{1/n}\left(\frac{\overline{\varphi}/\gamma_Y^*}{n-1}\right)^{(n-1)/n}} = \sigma_{C0}(1-D) \tag{8}$$

Here, $D = 1 - G^D/G$ is introduced as a measure of the accumulated damage to the shear modulus from the off-axis loads. This allows the strength to be expressed in terms of the uniaxial compression strength, σ_{C0}, and a shear damage term, $(1 - D)$, which is in agreement with the observations by Eyer et al. in Ref. [29] that the loss of longitudinal compression strength in CFRP tubes was directly proportionally to the loss of rigidity in the shear modulus.

While the above is admittedly a simplification of the true micromechanics of the problem, the aim here was to highlight the shortcomings in the current theory and investigate an alternative assumption for the material behaviour under off-axis compression until the micro-scale failure mechanisms are better understood.

In order to test this new assumption, the above criterion was implemented in MATLAB using the rate-dependent nonlinear shear properties obtained in section 4.1. As an initial approximation, since no cyclic loading data was available to calibrate the progressive matrix damage in this material, the secant shear modulus of the composite was used as an estimate for the damaged shear modulus.

Therefore, the initial misalignment, $\overline{\varphi}$, was calibrated from the uniaxial quasi-static compression test, as was done in the previous sections, and the shear damage, D, for each off-axis test case was approximated by $D = 1 - G^D/G$, using as G^D the secant shear modulus from the Ramberg-Osgood curves, as illustrated in Fig. 8.

The results, shown in Fig. 11 below, agree remarkably well with the experimental data for both quasi-static and dynamic cases up to the 6° off-axis tests. At 10°, the dynamic test showed significantly higher longitudinal strength than predicted using this approach. However, the stresses used for this initial analysis were obtained from CLT and may not adequately represent the state of the material at large amounts of shear. In addition, this approach requires knowledge of progressive damage evolution and, based on the cyclic loading data from Ref. [30, 31], the assumption that G^D equals to the secant modulus may result in overly conservative predictions. For illustrative purposes, the resulting envelopes assuming only 50% of damage to the shear modulus, indicated by the dotted lines in Fig. 11, show how the predictions may change if the shear damage were calibrated differently.

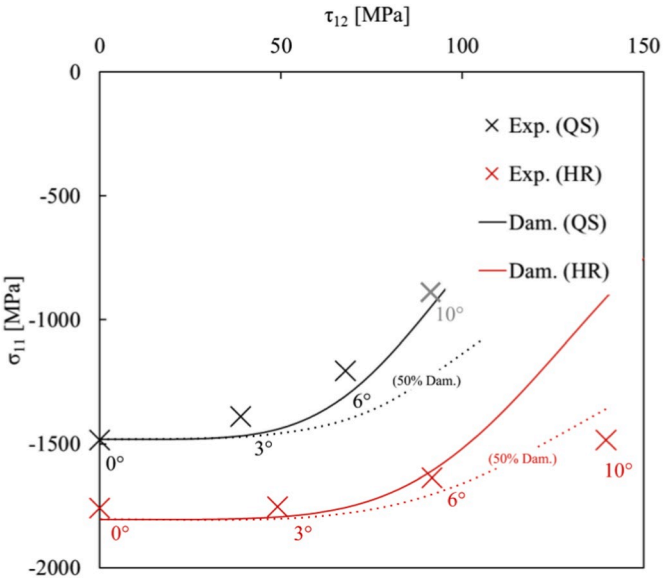

Fig. 11. *Predicted quasi-static and dynamic failure envelopes using proportional damaging of the shear modulus based on the constitutive model in* Ref. [32] *to predict the damage to the fibre kinking strength under multiaxial loads.*

Following the positive initial results from the preliminary analysis above, the proposed criterion was implemented into a user-defined material subroutine in LS-DYNA explicit finite element analysis (FEA) solver along with the rate- and pressure-dependent constitutive model described in Ref. [32] for a more in-depth evaluation. In this way, a more accurate representation of the stress states in the material could be obtained, as opposed to the analytical approximation obtained from the CLT, which only considers linear elastic behaviour. In addition, by using a multi-axial rate-dependent constitutive law for the nonlinear shear behaviour, both the uniaxial kinking strength, σ_{C0}, and the off-axis damage, D, in the proposed fibre kinking criterion, eq. (8), automatically become pressure-dependent as well as rate-dependent.

As was done in the previous analysis, the initial misalignment, $\overline{\varphi}$, was calibrated from the uniaxial quasi-static compression strength with all of the strain rate and off-axis effects deriving directly from the constitutive behaviour. However, since the finite element analysis produced a more accurate representation of the transverse and shear stresses present in the cross-ply material under uniaxial compression, a slightly different initial misalignment angle of 1.5° was obtained. For this, the constitutive model from Ref. [32] was calibrated for the IM7/8552 material using the off-axis transverse compression data in Refs. [23], allowing for the secant shear modulus to be extracted for any given stress state in order to determine the off-axis damage, D. A summary of the constitutive model and calibrated material properties can be found in Appendix A.

This model was then used to simulate each of the off-axis test cases at quasi-static and dynamic strain-rates. A simplified specimen geometry, shown in Fig. 12, was meshed using large 1 × 1x0.125 mm elements, to represent the central gauge section at a scale similar to what is typically used in industrial applications. The nodes on one end of the specimen were fixed in the axial direction and the opposite nodes were prescribed displacements at the average relative velocity between input and output bars for each of the test cases.

Finally, the different material orientations and prescribed velocities were applied for each test case and the simulations were run, extracting axial stress-strain curves from the total displacement and resultant force. A comparison between the stress-strain curves from the simulations and from the quasi-static [5] and dynamic experiments is shown in Fig. 13, below.

The FEA predictions obtained using the proposed criterion were,

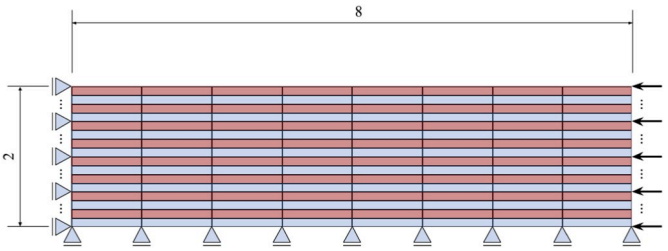

Fig. 12. Side view of the simplified FE mesh used to model the off-axis compression tests. Dimensions in mm.

again, in very good agreement with the experimental data, falling within the experimental scatter in all cases except the 10° quasi-static compression test. However, in this last case the model appeared to under predict the shear nonlinearity and thus the shear damage, which would result in an over prediction of the strength. In addition, in this case the model showed significant IFF damage before the fibre kinking strength was reached, meaning that beyond this point the kinking criterion would likely become irrelevant as matrix failure would dominate the material response at greater amounts of shear.

Therefore, while the proposed criterion may rely on more simplistic assumptions of the fibre kinking behaviour, the results from both the preliminary analysis and the FEA simulations suggest that Budiansky and Fleck's original assumptions for the off-axis loading behaviour likely overestimate its effects on fibre rotation in the misalignment frame. While further research will be required to determine the reasons for this and establish a more accurate description of the micromechanics of fibre kinking under multi-axial loading, the results indicate that, as an alternative, the assumption that off-axis loads do not significantly affect the fibre misalignment may be a closer approximation for the longitudinal compression failure of CFRP laminates under combined loading.

5. Conclusions

A series of high strain-rate compression tests have been performed on uniaxial and off-axis cross-ply IM7/8552 specimens. Along with previously reported quasi-static experiments on the same material [5], a comprehensive data set on the effects of shear and strain-rate on fibre kinking strength has been compiled. This new data has been used to evaluate leading fibre kinking theories [1–4,19], showing that, when coupled with rate-dependent nonlinear in-plane shear properties, they were able to accurately predict the effects of strain-rate on the longitudinal compression strength. However, none of the physically based kinking theories were able to capture the effects of shear, likely due to an over prediction of fibre rotation effects and indicating a need for better understanding of the micromechanics of kink band formation under multiaxial loads.

Instead, a simple shear damage model is proposed to account for the effect of off-axis stresses on the longitudinal compression strength, which relies on the alternative assumption that off-axis loads do not significantly affect the fibre misalignment. The proposed criterion was implemented in a user-defined material subroutine for LS-DYNA and used to model each of the reported test cases, showing very good agreement with the experimental results, both at quasi-static and dynamic strain-rates.

Therefore, until better knowledge of the micromechanics of kink band formation is obtained and the physically based theories can be updated, the simple more phenomenological approach is recommended for better predictions of the compression strength of FRP laminates under multiaxial loads.

authorship contribution statement

Daniel Thomson: Conceptualization, Methodology, Formal analysis, Software, Validation, Visualization, Writing - original draft, Writing - review & editing. **Gustavo Quino:** Methodology, Investigation. **Hao Cui:** Conceptualization, Methodology, Software, Validation. **Antonio Pellegrino:** Methodology, Investigation. **Borja Erice:**

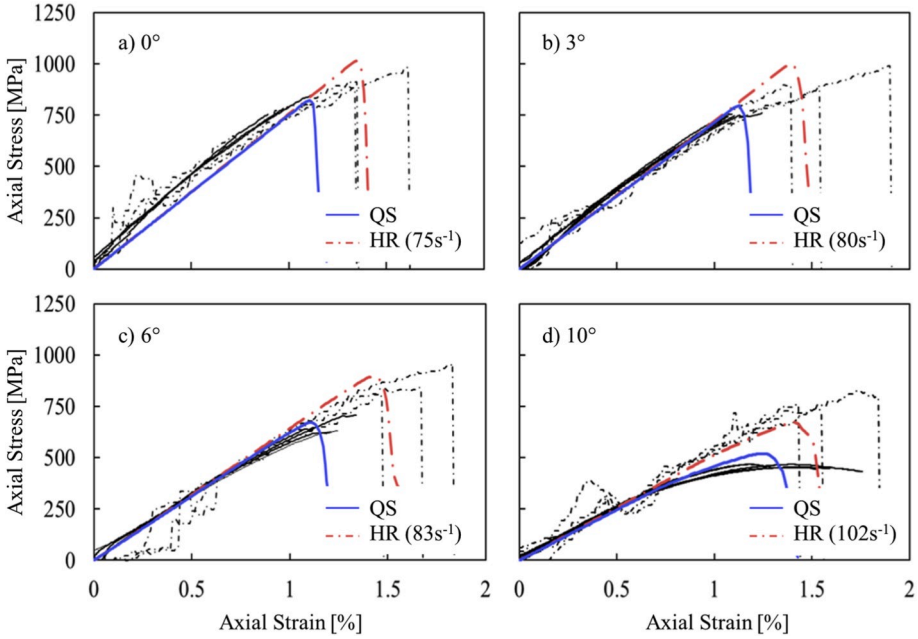

Fig. 13. Predicted axial stress-strain curves for each of the off-axis specimens at quasi-static (QS, solid blue) and dynamic (HR, dotted red) loading rates plotted over the QS (solid black) and HR (dotted black) experimental data from Fig. 4. (For interpretation of the references to colour in this figure legend, the reader is referred to the Web version of this article.)

Conceptualization, Methodology, Software, Validation, Visualization, Supervision. **Nik Petrinic:** Project administration, Funding acquisition, Resources, Supervision.

Acknowledgements

The authors would like to acknowledge Rolls-Royce plc, for their continuing support through the Solid Mechanics University Technology Centre at the University of Oxford.

Appendix A. Localisation plane plasticity model

In order to include strain rate and pressure effects in the FEA predictions, the proposed shear damage criterion for the off-axis compression strength was coupled with the following constitutive model originally presented in Ref. [32].

The model is based on the idea that the same physical phenomena behind Puck's failure criterion might also be able to explain the matrix-dominated nonlinear response observed in UD FRPs. Therefore, on the basis of Puck's IFF theory [33], the following localisation plane plasticity model is built on the assumption that the inelastic behaviour in these materials is caused by the shear stresses acting on a critical localisation plane around the fibre direction, Fig. 14, driven by a frictional Drucker-Prager-type equivalent stress.

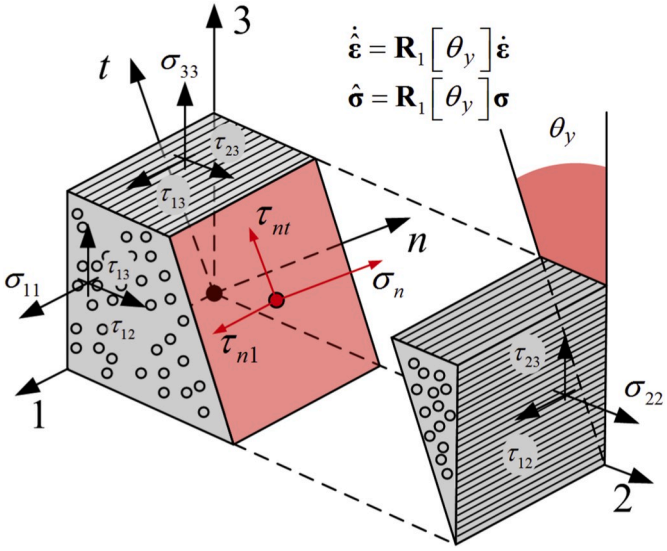

Fig. 14. Schematic view of the Puck localisation plane concept and rotation of the material aligned stresses around the fibre direction.

The yield function, that is proposed for the localisation plane (LP) plasticity model is expressed as:

$$f_y\left[\boldsymbol{\sigma}, \theta_y, \bar{\varepsilon}_p, \dot{\bar{\varepsilon}}_p\right] = f_y\left[\ \hat{\boldsymbol{\sigma}}, \bar{\varepsilon}_p, \dot{\bar{\varepsilon}}_p\right] = \bar{\sigma}\left[\ \hat{\boldsymbol{\sigma}}\right] - \tau_y\left[\bar{\varepsilon}_p\right] r_y\left[\dot{\bar{\varepsilon}}\right] = 0 \tag{9}$$

where $\tau_y[\bar{\varepsilon}_p]$ represents the strain hardening and $r[\dot{\bar{\varepsilon}}]$ the strain rate effects as described by eq. (2) in section 4.1. The term $\bar{\sigma}[\hat{\boldsymbol{\sigma}}]$ represents the equivalent stress on the localisation plane, θ_y, determined by the linear Drucker-Prager type expression, $\bar{\sigma}[\hat{\boldsymbol{\sigma}}] = \alpha\sigma_n + \sqrt{\tau_{n1}^2 + e\tau_{nt}^2}$, where the parameters α and e, respectively, represent the frictional coefficient that accounts for the pressure-dependency and a shear interaction parameter that accounts for the anisotropic behaviour along and transverse to the fibres.

The localisation plane stress components in this criterion, $\hat{\boldsymbol{\sigma}} = \{\sigma_1\sigma_n\sigma_t\tau_{n1}\tau_{nt}\tau_{1t}\}^T$, are obtained by the rotating the material stress tensor, $\boldsymbol{\sigma} = \{\sigma_{11}\sigma_{22}\sigma_{33}\tau_{12}\tau_{23}\tau_{13}\}^T$, around the fibre direction onto the potential yield plane, θ, using the rotation matrix $\boldsymbol{R}[\theta]$, following same approach used in the Puck IFF theory:

$$\hat{\boldsymbol{\sigma}} = \boldsymbol{R}\sigma, \quad \boldsymbol{R}[\theta] = \begin{bmatrix} 1 & 0 & 0 & 0 & 0 & 0 \\ 0 & c^2 & s^2 & 0 & 2sc & 0 \\ 0 & s^2 & c^2 & 0 & -2sc & 0 \\ 0 & 0 & 0 & c & 0 & s \\ 0 & -cs & cs & 0 & c^2 - s^2 & 0 \\ 0 & 0 & 0 & -s & 0 & c \end{bmatrix}, \quad \text{where} \begin{array}{l} c = \cos[\theta] \\ s = \sin[\theta] \end{array} \tag{10}$$

The flow rule is chosen to be non-associative as generally is in most of the pressure-dependent plasticity models:

$$g[\hat{\boldsymbol{\sigma}}] = \alpha_g\sigma_n + \sqrt{\tau_{n1}^2 + e_g\tau_{nt}^2} \tag{11}$$

The hardening of the material is modelled as purely isotropic. For the sake of simplicity, no kinematic or distortional hardening is considered. In order to do so, a combined Voce strain hardening and strain rate hardening is defined as a function of the equivalent plastic strain and equivalent plastic strain rate as:

$$\tau_y[\varepsilon_p]\, r_y[\dot{\varepsilon}] = \left\{A + B_1\left(1 - e^{[-C_1\varepsilon^p]}\right) + B_2\left(1 - e^{[-C_2\varepsilon^p]}\right)\right\}\left\{1 + \sqrt{K_y\dot{\varepsilon}}\right\} \quad (12)$$

where K_y is the strain rate coefficient, A is the initial yield stress and B_1, C_1, B_2, and C_2, are the strain hardening material constants. The strain hardening and the strain rate hardening effects have been considered independent for the sake of simplicity and ease of calibration.

The model, which is explained in more detail in Refs. [32,34], was implemented as a user-defined material subroutine in the LS-DYNA explicit FEA solver and calibrated with the properties given in Table 3 to fit the nonlinear stress-strain curves of the IM7/8552 material from Ref. [23].

Table 3
Constitutive model parameters used to describe the nonlinear behaviour of IM7/8552, calibrated from the data given in Ref. [23].

Plastic Properties									
A	B_1	C_1	B_2	C_2	α	α_g	e	e_g	K_y
60	33	130	25	10	0.1	0.23	0.9	1	1E-03

References

[1] B. Budiansky, N.A. Fleck, Compressive failure of fibre composites, J. Mech. Phys. Solid. 41 (1993) 183–211, https://doi.org/10.1016/0022-5096(93)90068-Q.
[2] N.A. Fleck, Compressive failure of fiber composites, Adv. Appl. Mech. 33 (1997).
[3] S.T. Pinho, Modelling Failure of Laminated Composites Using Physically-Based Failure Models, 2005.
[4] S.T. Pinho, L. Iannucci, P. Robinson, Physically-based failure models and criteria for laminated fibre-reinforced composites . Part I: Development, Compos Part A Appl Sci Manuf 37 (2006) 63–73, https://doi.org/10.1016/j.compositesa.2005.04.016.
[5] D. Thomson, H. Cui, B. Erice, N. Petrinic, A study on the longitudinal compression strength of fibre reinforced composites under uniaxial and off-axis loads using cross-ply laminate specimens, Compos Part A Appl Sci Manuf 121 (2019) 213–222, https://doi.org/10.1016/j.compositesa.2019.03.034.
[6] T. Matsuo, K. Kageyama, Compressive failure mechanism and strength of unidirectional thermoplastic composites based on modified kink band model, Compos Part A Appl Sci Manuf 93 (2017) 117–125, https://doi.org/10.1016/j.compositesa.2016.11.018.
[7] M. Ploeckl, P. Kuhn, J. Grosser, M. Wolfahrt, H. Koerber, A dynamic test methodology for analyzing the strain-rate effect on the longitudinal compressive behavior of fiber-reinforced composites, Compos. Struct. 180 (2017) 429–438, https://doi.org/10.1016/j.compstruct.2017.08.048.
[8] J.S. Welsh, D.F. Adams, Testing of angle-ply laminates to obtain unidirectional composite compression strengths, Compos Part A Appl Sci Manuf 28 (1997) 387–396, https://doi.org/10.1016/S1359-835X(96)00138-8.
[9] Hexcel HexPly 8552 Data Sheet. n.d.
[10] S.W. Yurgartis, Measurement of small angle fiber misalignments in continuous fiber composites, Compos. Sci. Technol. 30 (1987) 279–293, https://doi.org/10.1016/0266-3538(87)90016-9.
[11] C.A. Schneider, W.S. Rasband, K.W. Eliceiri, NIH Image to ImageJ: 25 years of image analysis, Nat. Methods 9 (2012) 671–675, https://doi.org/10.1038/nmeth.2089.
[12] HexTow ® IM7 Carbon Fiber, 2018.
[13] M.W. Czabaj, M.L. Riccio, W.W. Whitacre, Numerical reconstruction of graphite/epoxy composite microstructure based on sub-micron resolution X-ray computed tomography, Compos. Sci. Technol. 105 (2014) 174–182, https://doi.org/10.1016/J.COMPSCITECH.2014.10.017.
[14] Y. Wang, T.L. Burnett, Y. Chai, C. Soutis, P.J. Hogg, P.J. Withers, X-ray computed tomography study of kink bands in unidirectional composites, Compos. Struct. 160 (2017) 917–924, https://doi.org/10.1016/j.compstruct.2016.10.124.
[15] H. Cui, D. Thomson, A. Pellegrino, J. Wiegand, N. Petrinic, Effect of strain rate and fibre rotation on the in-plane shear response of ±45° laminates in tension and compression tests, Compos. Sci. Technol. 135 (2016) 106–115, https://doi.org/10.1016/j.compscitech.2016.09.016.
[16] G. Quino, A. Pellegrino, V.L. Tagarielli, N. Petrinic, Measurements of the effects of pure and salt water absorption on the rate-dependent response of an epoxy matrix, Compos. B Eng. 146 (2018) 213–221, https://doi.org/10.1016/j.compositesb.2018.03.044.
[17] M.J. Shuart, Failure of compression-loaded multidirectional composite laminates, AIAA J. 27 (1989) 1274–1279, https://doi.org/10.2514/3.10255.
[18] P.D. Soden, M.J. Hinton, A.S. Kaddour, Biaxial test results for strength and deformation of a range of E-glass and carbon fibre reinforced composite laminates: failure exercise benchmark data, Compos. Sci. Technol. 62 (2002) 1489–1514, https://doi.org/10.1016/S0266-3538(02)00093-3.
[19] Pinho ST, Dávila CG, Camanho PP, Iannucci L, Robinson P. Failure Models and Criteria for FRP under In-Plane or Three-Dimensional Stress States Including Shear Non-linearity. Nasa/Tm-2005-213530 2005:68. doi:NASA/TM-2005-213530.
[20] H. Körber, Mechanical Response of Advanced Composites under High Strain Rates, University of Porto, 2010.
[21] J. Wiegand, N. Petrinic, Constitutive modelling of composite materials under impact loading, Dep Eng Sci (2009) 251. D. Phil.
[22] R. Gerlach, C.R. Siviour, N. Petrinic, J. Wiegand, Experimental characterisation and constitutive modelling of RTM-6 resin under impact loading, Polymer (2008), https://doi.org/10.1016/j.polymer.2008.04.018.
[23] H. Koerber, J. Xavier, P.P. Camanho, High strain rate characterisation of unidirectional carbon-epoxy IM7-8552 in transverse compression and in-plane shear using digital image correlation, Mech. Mater. 42 (2010) 1004–1019, https://doi.org/10.1016/j.mechmat.2010.09.003.
[24] W. Ramberg, W.R. Osgood, Description of Stress-Strain Curves by Three Parameters, 1943.
[25] B.W. Rosen, Mechanics of Composite Strengthening. Fiber Compos. Mater. Semin. Am. Soc. Met., American Society for Metals, Ohio, 1965, pp. 37–75.
[26] A.S. Argon, Fracture of composites, Treatise Mater Sci Technol 1 (1972) 79–114, https://doi.org/10.1016/B978-0-12-341801-2.50007-2.
[27] W.S. Slaughter, N.A. Fleck, B. Budiansky, Compressive failure of fiber composites: the roles of multiaxial loading and creep, J. Eng. Mater. Technol. 115 (1993) 308, https://doi.org/10.1115/1.2904223.
[28] F. Naya, M. Herráez, C.S. Lopes, C. González, S. Van der Veen, F. Pons, Computational micromechanics of fiber kinking in unidirectional FRP under different environmental conditions, Compos. Sci. Technol. 144 (2017) 26–35, https://doi.org/10.1016/J.COMPSCITECH.2017.03.014.
[29] G. Eyer, O. Montagnier, C. Hochard, J.-P. Charles, Effect of matrix damage on compressive strength in the fiber direction for laminated composites, Compos Part A Appl Sci Manuf 94 (2017) 86–92, https://doi.org/10.1016/j.compositesa.2016.12.012.
[30] S. Treutenaere, Modelling of the Fabric Reinforced Polymers Behaviour with Delamination Prediction for Impact-type Loading, 2016.
[31] M.C. Lafarie-Frenot, F. Touchard, Comparative in-plane shear behaviour of long-carbon-fibre composites with thermoset or thermoplastic matrix, Compos. Sci. Technol. 52 (1994) 417–425, https://doi.org/10.1016/0266-3538(94)90176-7.
[32] D.M. Thomson, B. Erice, H. Cui, J. Hoffmann, J. Wiegand, N. Petrinic, A Puck-based localisation plane theory for rate- and pressure-dependent constitutive modelling of unidirectional fibre-reinforced polymers, Compos. Struct. 184 (2018) 299–305, https://doi.org/10.1016/j.compstruct.2017.09.088.
[33] A. Puck, H. Schürmann, Failure analysis of FRP laminates by means of physically based phenomenological models, Compos. Sci. Technol. 58 (1998) 1045–1067, https://doi.org/10.1016/S0266-3538(96)00140-6.
[34] B. Erice, D. Thomson, S.A. Ponnusami, M.V. Pathan, N. Petrinic, On the rate-dependent plasticity modelling of unidirectional fibre-reinforced polymeric matrix composites, EPJ Web Conf. 183 (2018), 01055, https://doi.org/10.1051/epjconf/201818301055.